Structures of the ATP-fueled ClpXP proteolytic machine bound to protein substrate

Xue Fei[1], Tristan A Bell[1], Simon Jenni[2], Benjamin M Stinson[1], Tania A Baker[1,3], Stephen C Harrison[2,3], and Robert T Sauer[1,*]

[1]Department of Biology, Massachusetts Institute of Technology, Cambridge, MA 02139

[2]Department of Biological Chemistry and Molecular Pharmacology, Harvard Medical School, Boston, MA 02115

[3]Howard Hughes Medical Institute.

* Correspondence; bobsauer@mit.edu

running head: Cryo-EM ClpXP structures

ClpXP is an ATP-dependent protease in which the ClpX AAA+ motor binds, unfolds, and translocates specific protein substrates into the degradation chamber of ClpP. We present cryo-EM studies that show how asymmetric hexameric rings of ClpX bind symmetric heptameric rings of ClpP and interact with protein substrates. Subunits in the ClpX hexamer assume a spiral conformation and interact with two-residue segments of substrate in the axial channel. Other AAA+ proteases and protein-remodeling machines have similar structures, and strictly sequential models of ATP hydrolysis and a power stroke that moves two residues of the substrate per translocation step have been inferred from these structural features. However, biochemical and single-molecule biophysical studies indicate that ClpXP operates by a probabilistic mechanism in which 5 to 8 residues are translocated for each ATP hydrolyzed. Thus, our results suggest that structurally similar AAA+ machines operate by a ClpX-like mechanism.

AAA+ motors harness the energy of ATP hydrolysis to carry out mechanical tasks in cells[1]. For example, AAA+ ClpX ring hexamers bind target proteins, unfold them, and then translocate the unfolded polypeptide through an axial channel and into the chamber of the tetradecameric ClpP peptidase for degradation (**Fig. 1a**)[2]. ClpX, HslU, and Lon are members of the HCLR clade of protease motors, whereas YME1/FtsH and proteasomal Rpt_{1-6}/PAN are classic-clade motors[1]. Both clades include structurally conserved large and small AAA+ domains and a variety of sequence motifs that mediate ATP binding and hydrolysis as well as protease and substrate recognition (**Fig. 1b**).

Cryo-EM structures of AAA+ proteases and protein-remodeling machines, largely members of the classic clade, show that subunits in the hexameric motor assume spiral conformations, typically with axial pore-1 loops from successive subunits interacting with two-residue segments of a substrate in the axial channel, suggesting that translocation occurs in two-residue steps[3–14].

By contrast, the smallest ClpXP translocation steps observed in single-molecule optical-trapping experiments correspond to movement of 5 to 8 amino acids of the substrate, and kinetic bursts of power strokes produce movements two, three, or four-fold larger in terms of the number of residues translocated[15-19]. This discrepancy suggests either that ClpX interacts with substrates in a different manner, or that all protease motors function by similar mechanisms that result in larger translocation steps and bursts. Here, we present cryo-EM structures of ClpXP complexes bound to protein substrates that support the second model.

RESULTS AND DISCUSSION

EM structures

Single-chain $ClpX^{\Delta N}$ contains six subunits, each lacking the N domain, which are connected by tethers and bind ClpP to form an active ATP-dependent protease[20]. For cryo-EM studies, we used epitope-tagged variants of *Escherichia coli* ClpP and a single-chain variant of *E. coli* $ClpX^{\Delta N}$ with an E185Q mutation to eliminate ATP hydrolysis without compromising nucleotide, ClpP, or substrate binding[20–21]. We purified enzymes separately and incubated $ClpX^{\Delta N}$ (4 μM pseudohexamer), ClpP (2 μM 14-mer), and ATPγS (5 mM) for 5 min before vitrification. Imaging revealed complexes with ClpP bound to one or two $ClpX^{\Delta N}$ hexamers (**Supplementary Fig. 1**). We analyzed the more abundant doubly capped complexes. As single-particle data processing with C_2 symmetry produced maps with conformational heterogeneity, we subtracted density from $ClpX^{\Delta N}$ or ClpP to allow independent classification and refinement (**Supplementary Figs. 1-2**). We calculated a D_7 symmetric map for ClpP and parts of $ClpX^{\Delta N}$ making symmetric contacts, four different classes of symmetry-free $ClpX^{\Delta N}$ maps, and then extended each asymmetric $ClpX^{\Delta N}$ map to include one heptameric ClpP ring (**Supplementary Fig. 2**). Final structures have good stereochemistry with resolutions from 3.2 to 4.3 Å (**Supplementary Table 1**). Substrates were observed in all $ClpX^{\Delta N}$ structures and probably represent endogenous

peptides/proteins bound by ATPase-inactive ^{E185Q}ClpX$^{\Delta N}$ hexamers or partially denatured portions of ClpP or ClpX$^{\Delta N}$.

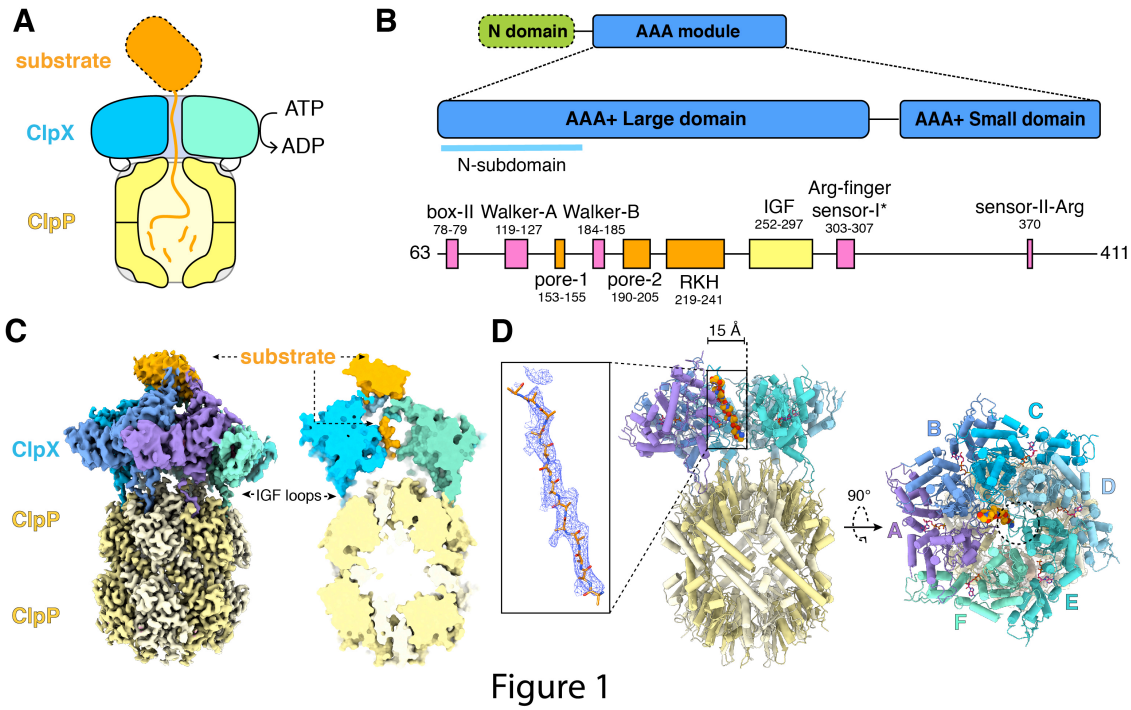

Figure 1 ClpXP protease**.** (**a**) Schematic representation of ClpXP. (**b**) ClpX domain structure and positions of sequence motifs important for ATP binding and hydrolysis (magenta), substrate binding (orange), and ClpP binding (yellow). (**c**) Left. Composite cryo-EM density of ClpX$^{\Delta N}$/ClpP complex. ClpP is yellow; ClpX$^{\Delta N}$ (class 3) is blue, green, or purple; substrate is orange; and nucleotide is red. Right. Slice through density showing substrate in the axial channel and ClpP degradation channel. (**d**) Left. Cartoon representation of the class-4 ClpX$^{\Delta N}$ hexamer (subunit F removed) and its docking with a heptameric ClpP ring. Substrate in the ClpX channel is shown in space-filling representation as a poly-alanine chain; the inset shows substrate as a ball-and-stick model with associated density. The dashed line shows the 7-fold symmetry axis of ClpP. Right. View rotated by 90°. The dashed circle shows the position of the ClpP pore.

Fig. 1c shows density for a composite ClpX$^{\Delta N}$/ClpP/substrate complex. The six subunits of ClpX$^{\Delta N}$ formed a shallow spiral (labeled ABCDEF from top to bottom) in all structural classes, which differed largely in substrate density or nucleotide state, and the hexameric ClpX$^{\Delta N}$ and heptameric ClpP rings were slightly offset (**Fig. 1d**). The structures of ClpX$^{\Delta N}$ hexamers in our

EM structures were similar to each other (pair-wise Cα RMSD 1.2-2.3 Å) but different than non-spiral crystal structures of $ClpX^{\Delta N}$ lacking substrate and ClpP[22–23].

ClpX docking with ClpP

Our D_7 map included $ClpP_{14}$ and symmetric interface contacts with $ClpX^{\Delta N}$ (**Fig. 2a**). In both heptameric ClpP rings, the N-terminal residues of each subunit formed a collar of β-hairpins creating a pore into the degradation chamber (**Fig. 2b; Supplementary Fig. 3**). ClpP had essentially the same structure in the D_7 and symmetry-free maps. ClpX IGF loops, named for an Ile^{268}-Gly^{269}-Phe^{270} sequence, are critical for ClpP binding[24–27] and were responsible for most contacts in our structures (**Fig. 2c**). These interactions included packing of the Ile^{268}, Phe^{270}, and Val^{274} side chains into pockets near interfaces between ClpP subunits (**Fig. 2d**); I268L, F270L, and V274A variants have severe ClpP binding defects[27]. Asymmetric ClpX-ClpP docking relies on conformational adjustments in the N- and C-terminal residues of individual IGF loops, allowing the central portion of each IGF loop to contact the flat ClpP ring despite projecting from a spiral (**Fig. 2e**). In the symmetry-free maps, the unoccupied pocket in each ClpP heptamer was always located between the pockets bound by IGF loops from ClpX subunits E and F (**Supplementary Fig. 3 and movie 1**).

Our structures included hydrogen bonds between the side chain of Arg^{192} in ClpP and the backbone of the IGF loop, which are likely to be important for binding (**Fig. 2f)**. Indeed, we found that ^{R192K}ClpP did not degrade protein substrate in the presence of $ClpX^{\Delta N}$ (**Fig. 2g, left**), and unlike wild-type ClpP, did not suppress the ATPase activity of $ClpX^{\Delta N}$ (**Fig. 2g, middle**). Small-molecule acyldepsipeptides (ADEPs) bind in the same ClpP pockets as the ClpX IGF loops and kill bacteria by opening the ClpP pore to facilitate rogue degradation of large peptides and unstructured proteins[28–31]. ADEPs stimulated R192K and wild-type ClpP decapeptide cleavage to similar extents (**Fig. 2g, right**), establishing that ^{R192K}ClpP has normal catalytic

activity. Thus, Arg[192] is critical for ClpX recognition but not for ADEP binding or ClpP pore opening. Modifying ADEPs to interact with Arg[192] may increase affinity for ClpP and improve their efficacy as antibiotics.

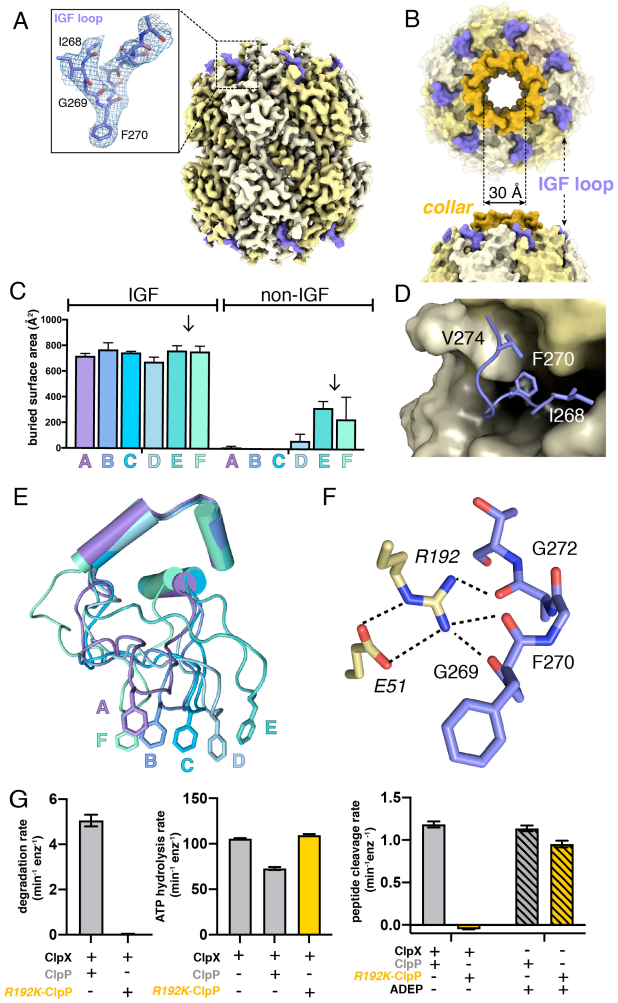

Figure 2

Figure 2 ClpP and symmetric IGF loop contacts. (**a**) Density for $ClpP_{14}$ in the D_7 map is shown in yellow. Density for part of the IGF loops of ClpX is shown in blue. The inset shows the density as mesh and the fitted model for residues 267-275 of one IGF loop. (**b**) Top views of ClpP showing the axial collar (darker yellow) and pore. (**c**) IGF loops of ClpX make the majority of contacts with ClpP as assessed by buried surface area. Each bar represents a different $ClpX^{\Delta N}$ subunit in the spiral and values are means ± 1 SD for the four classes. The arrows between subunits E and F mark the position of the unoccupied ClpP cleft. (**d**) The side chains of IGF residues Ile[268] (I268) Phe[270] (F270), and Val[274] (V274) pack into hydrophobic ClpP clefts. (**e**) After alignment of the large AAA+ cores of the six subunits in the class-4 $ClpX^{\Delta N}$ hexamer, the IGF loops adopt a variety of conformations, helping mediate ClpP binding despite the symmetry mismatch. (**f**) The side chain of Arg[192] (*R192*) in ClpP makes hydrogen bonds with carbonyl oxygens in the IGF loop of ClpX and also makes a salt bridge with Glu[51] (*E51*) in a neighboring

ClpP subunit. (**g**) Left – ClpX$^{\Delta N}$ supports degradation of ^{cp7}GFP-ssrA by ClpP but not ^{R192K}ClpP. Middle – ClpP but not ^{R192K}ClpP suppresses ATP hydrolysis by ClpX$^{\Delta N}$. Right – ClpX$^{\Delta N}$ supports degradation of a decapeptide by ClpP but not ^{R192K}ClpP. ADEP-2b activates decapeptide cleavage by both ClpP and ^{R192K}ClpP. Error bars represent means (n=3) ± 1 SD.

Substrate binding

All ClpX$^{\Delta N}$ maps contained substrate density within the axial channel, which we modeled as an extended poly-alanine chain (**Fig. 1d**) except for a few residues. The class-1 and class-3 structures also had density corresponding to a roughly globular native domain above the channel (**Fig. 1c; Supplementary Fig. S4**). The pore-1, pore-2, and RKH loops of ClpX contacted substrate, in accord with genetic and biochemical studies[32–38]. For example, the pore-1 loops of subunits B, C, D, and E interacted with substrate in the channels of all classes, whereas these loops from subunits A and F did so only in some classes (**Figs. 3a-3c; Supplementary Fig. 4 and movie 2**). For each engaged pore-1 loop, the side chains of Tyr^{153} and Val^{154} packed between β-carbons spaced two-residues apart on opposite sides of the extended substrate (**Figs. 3a-b; Supplementary Fig. 4 and movie 2**). Mutation of pore-1 side chains alters substrate grip and interferes with normal translocation and unfolding[32,35–38]. Interactions near the top of the ClpX channel are most important for substrate grip during unfolding[39], and this region of the channel was most constricted (**Figs. 1d, 3a, Supplementary Fig. 5**). Depending on the class, from three to five pore-2 loops also contacted substrate, with Arg^{200} making most contacts (**Figs. 3a, 3c; Supplementary movie 2**). The arrangement of pore-1 and pore-2 loops and their interactions with substrate were similar to those in other AAA+ protein unfolding and remodeling machines[3–14].

The RKH loop is unique in ClpX-family enzymes[40] and consisted of an antiparallel β-ribbon stem and a short helix that includes part of the conserved Arg^{228}-Lys^{229}-His^{230} motif (**Fig. 3d**). Most RKH loops had reasonable density and mimicked adjustable structural jacks supporting a house during foundation repair when contacting substrate above the pore (**Fig. 3d**). The RKH loops

influence substrate specificity[33–34], but it is not known if they are critical determinants of substrate binding. To test this possibility, we constructed and assayed RKH-loop mutants. The most severe mutant (RKH changed to AAA) did not support ClpP degradation and hydrolyzed ATP ~5-fold faster than the parent (**Figs. 3e, 3f**). Changing RKH to AKH, KHR, or KRH slowed degradation (**Fig. 3g**). A variant $[RKH_2\text{-}AAA]_2$ pseudohexamer with four wild-type RKH loops and two AAA mutations had a ~3-fold higher K_M for substrate degradation than the parent and hydrolyzed ATP slightly faster (**Figs. 3f, 3g**). Thus, the RKH loops play important roles in substrate recognition and regulating rates of ATP hydrolysis.

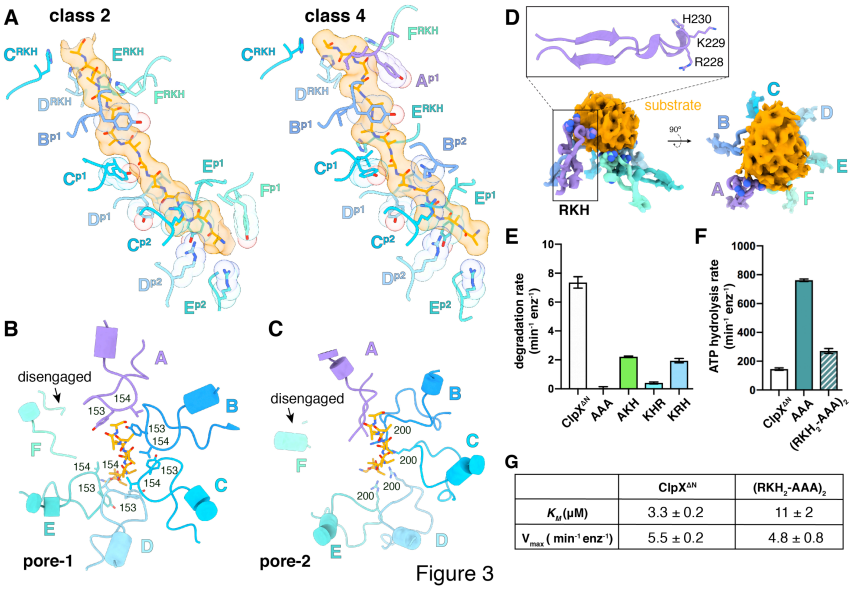

Figure 3 Substrate contacts. (**a**) Interaction of substrate (orange, stick and surface representation) in the class-2 and class-4 structures with loops (blue and purple, stick and transparent space-filling representation) in the axial channel of $ClpX^{\Delta N}$. Capital letters indicate subunits; superscripts indicate RKH loops, pore-1 (p1) loops, or pore-2 (p2) loops. (**b**) Top view of interactions of pore-1 loops with substrate (class 4). (**c**) Top view of interactions of pore-2 loops with substrate (class 4). (**d**) Interaction of RKH loops in the class-3 structure with the globular portion of the substrate above the channel. (**e**) Mutation of RKH motifs in each subunit of a $ClpX^{\Delta N}$ hexamer inhibits degradation of Arc-st11-ssrA. (**f**) Effects of RKH mutations on ATP hydrolysis. (**g**) Mutating two RKH motifs in a single chain pseudohexamer to AAA increases K_M for steady-state degradation of ^{CP7}GFP-ssrA.

Nucleotide binding and motor conformations

We observed electron density for five ATPγS molecules and one ADP in each ClpX$^{\Delta N}$ hexamer (see, for example, **Figs. 4a, 4b; Supplementary Table 2**). ADP was bound either in subunit A (class 2) or subunit F (classes 1, 3 and 4); these subunits made fewer contacts with their ATP-bound neighbors and were offset from the axis of the hexamer by ~2.5 Å (**Figs. 4c-4e; Supplementary Table 3**).

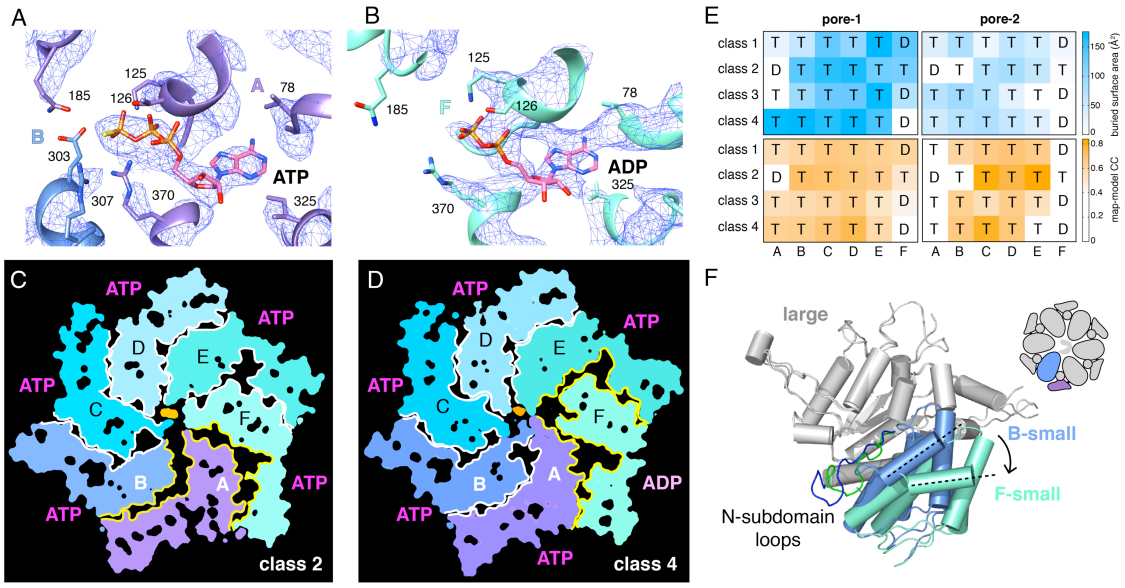

Figure 4

Figure 4 Nucleotide binding and subunit interactions in ClpX$^{\Delta N}$ hexamers. (**a**) Density for ATPγS in subunit A of the class-4 hexamer. The positions of ATP-binding/hydrolysis motifs are shown in cartoon and stick representation. (**b**) ADP in subunit F of the class-4 hexamer. (**c**, **d**) Slices through the density maps of class-2 and class-4 hexamers show that the ADP-bound subunit (A or F, respectively) makes fewer neighbor contacts than ATP-bound subunits. (**e**) Contacts between substrate and pore-1 loops (left) or pore-2 loops (right) were characterized by buried surface area (top) or model-to-map correlation (bottom). T represents an ATP-bound subunit; D represents an ADP-bound subunit. (**f**) The small AAA+ domain of subunit F in the class-4 structure packs against the neighboring large AAA+ domain somewhat differently than other small domains, represented here by subunit B. The inset shows packing between neighboring large (subunit B) and small domains (subunit A).

Val[78]-Ile[79] (box-II), Lys[125]-Thr[126]-Leu[127] (Walker A), Asp[184]-Gln[185] (Walker B with E185Q mutation), Arg[307] (arginine finger), and Arg[370] (sensor-II) side chains contact most nucleotides (**Figs. 4a, 4b, Supplementary Fig. 6**). V78A/I79A, E185Q, and R370K mutations eliminate ATP hydrolysis or weaken nucleotide binding[20,21,23,25], and we found that K125M, T126A, L127A, D184A, and R307A mutations also severely inhibited ATP hydrolysis (**Supplementary Fig. 6**). In most sites, the side chain of Glu[303] was close to the nucleoside γ-thiophosphate, at a position similar to the sensor-I residue that helps position water for hydrolysis in many AAA+ enzymes[1]. An E303A mutation severely inhibited ATP hydrolysis, but E303Q did not (**Supplementary Fig. 6**). We refer to Glu[303] as a sensor-I* element. Glu[303] is in the same helix as Arg[307], the arginine-finger residue, and thus these residues could coordinate structurally to activate ATP hydrolysis in a neighboring subunit, whereas sensor-I elements activate hydrolysis within the same subunit[1].

A short hinge connects the large and small AAA+ domain of each ClpX$^{\Delta N}$ subunit. The structures of the small domains were very similar as were those of the large domains after removing an N-terminal subdomain (residues 65-114) and the pore-1, pore-2, RKH, and IGF loops (**Supplementary Fig. 7**). The relative orientations of the large and small AAA+ domains were similar across all four structural classes for subunits at equivalent spiral positions, but conformational changes in the hinge resulted in different domain-domain orientations at many positions in the spiral (**Supplementary Fig. 7**). Changes in hinge length or deletion of one hinge largely eliminate ClpX function[41–42]. Thus, the conformational changes associated with a power stroke likely arise from changes in hinge conformations, whereas movements of different large-domain loops or the N-subdomain mediate ring closure and asymmetric contacts with ClpP and substrate.

ATP hydrolysis requires positioning: (*i*) the box-II, Walker-A, and Walker-B elements in the large AAA+ domain of one subunit; (*ii*) the sensor-II arginine from the small AAA+ domain of the same subunit; and (*iii*) the arginine-finger/sensor-I* element from the large domain of the clockwise subunit (viewed from the top of the ring). Whether an ATP-binding site is active or inactive with respect to hydrolysis appears to roughly correlate with how tightly the small AAA+ domain of each subunit packs against the large AAA+ domain of its clockwise neighbor. These small-domain/large-domain interfaces were similar for units A/B, B/C, C/D, D/E, and E/F, and the associated nucleotide-binding sites were potentially all catalytically active for ATP hydrolysis. The FA interface was somewhat different (**Fig. 4f**), resulting in disengagement of the Arg-finger and sensor-I* side chains in subunit A from the nucleotide bound to subunit F (**Fig. 4b; Supplementary Table 4**). These observations suggest that the nucleotide-binding site in subunit F is catalytically inactive. Small changes contribute to the different F/A packing interface, including changes in rotation of the N-subdomain in subunit A relative to the rest of the large AAA+ domain, and changes in a loop that contains the sensor-II arginine in subunit F (**Fig. 4f**).

Implications for translocation models

Strictly sequential models have been proposed for the classic-clade AAA+ Yme1 protease and the Rpt_{1-6} ring of the 26S proteasome[3–5]. Based on the nucleotide and substrate-engagement states of different subunits, these models place distinct cryo-EM structures in a defined kinetic pathway in which ATP hydrolysis in the fifth spiral subunit (subunit E in ClpX) drives a power stroke that moves each subunit to a position offset by +1 from its previous location (i.e., subunits ABCDEF move to positions BCDEFA), generating a two-residue translocation step (**Fig. 5a**). We refer to this proposed model as the "classic-clade" mechanism. Although ClpX is a member of the HCLR clade, the structures reported here resemble those of Yme1 and Rpt_{1-6} in the spiral architecture of the hexamer, the positions of subunits that contain a nucleoside

triphosphate, the interaction of successive pore-1 loops with two-residue segments of the substrate, and the patterns of substrate engaged and disengaged pore-1 and pore-2 loops in the ring[3–5]. Thus, based on structure alone, ClpXP might also be expected to operate by a strictly sequential mechanism with a two-residue power stroke. However, multiple experimental observations are at odds with this model.

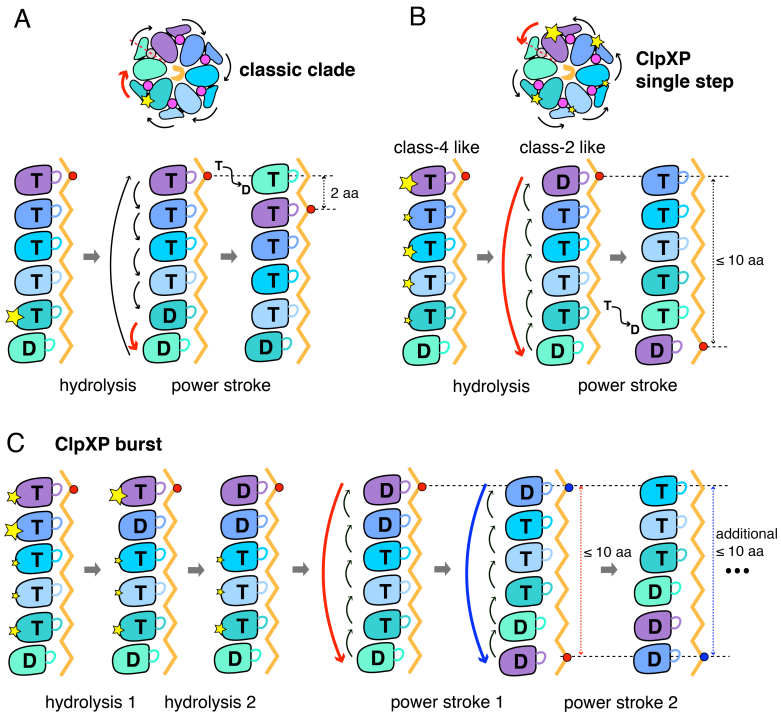

Figure 5 Translocation models. (**a**) Strictly sequential translocation model with a two-residue step proposed for the classic-clade Yme1 protease and 26S proteasome[3–5]. Only subunit E is hydrolytically active (depicted by star). Hydrolysis and/or subsequent product release results in a two-residue translocation step, in which the top five subunits in the spiral move down one position and the bottom subunit moves up to the top position. (**b**) Model in which ATP hydrolysis and/or product release in subunit A (depicted by large star) generates a power stroke that moves this subunit to position F, dragging substrate with it, and subunits BCDEF move up one position to become ABCDE. This model generates a translocation step of as many as 10 residues. Smaller stars indicate some probability of ATP hydrolysis occurring in other subunits, as illustrated in the next panel. (**c**) Initial ATP hydrolysis in subunit B generates strain but no power stroke. Hydrolysis in subunit A then drives one power stroke (like that depicted in panel B). The consequent movement of subunit B into the A position then drives a second power stroke, resulting in a kinetic burst of two translocation steps. In all panels, T represents ATP-bound subunits, and D represents subunits containing ADP and possibly inorganic phosphate.

First, the basic translocation step of ClpXP is ~1 nm in optical-trapping experiments[15–19]. In these experiments, step size is measured as the average distance an unfolded polypeptide moves between successive translocation steps and is converted into amino-acid residues using the wormlike-chain model. At the trapping forces employed, ~1 nm corresponds to 5-8 amino acids. This ~1-nm distance should not be confused with the ~0.6 nm distance between pore-1 loop contacts with substrate in the axial channel, as binding enforces an extended rather than partially compact polypeptide conformation. ClpXP also translocates polyproline[43], which cannot form an extended β structure. Thus, additional modes of ClpX interaction with substrate in the channel must exist, raising the possibility that translocation steps need not occur in quantized multiples of two-residue units. Substrate slipping could also reduce translocation step sizes.

Second, ClpXP translocation bursts as long as ~4 nm are occasionally observed in optical trapping-experiments, corresponding to movements of 20 to 32 residues through the channel in 20 ms or less[15–19]. In the classic-clade model, this would require 10 or more independent power strokes, each requiring distinct ADP release and ATP rebinding steps. Under the conditions used for optical trapping, we established that the steady-state rate of $ClpX^{\Delta N}$/ClpP ATP hydrolysis is 3.6 ± 0.1 s^{-1} (**Supplementary Fig. 8**) corresponding to a time constant of ~280 ms. Thus, on average, more than 2 s would be required for ClpXP to sequentially bind and release 10 ATPs, making it unlikely that it functions by the classic-clade mechanism.

Third, only one subunit in the spiral can hydrolyze ATP in the classic-clade model. If ClpX operated in this fashion, then single-chain variants containing subunits that cannot hydrolyze ATP should stall when an ATPase inactive subunit moves into the hydrolysis position. However, $ClpX^{\Delta N}$ hexamers with just two ATPase-active subunits support ClpP degradation at ~30% of the wild-type rate[20]. It might be argued that thermal motions move an ATPase-inactive subunit

out of the hydrolysis position in the ClpX spiral and an active subunit into it, thereby allowing continued function. We cannot exclude this possibility, but it seems unlikely in the absence of other factors, as the variant with just two ATPase active subunits translocates against forces as high as 10 pN in optical-trap experiments[18]. An alternative model is that ATP hydrolysis in the ClpX hexamer is probabilistic, in the sense that subunits at various positions in the spiral can hydrolyze ATP[18,20]. Consistent with this proposal, only subunit F appears to be catalytically inactive in our ClpX structures.

How certain is a strictly sequential mechanism with a two-residue translocation step for classic-clade AAA+ proteases? To our knowledge, no experiments establish the translocation step size for these enzymes. Moreover, classic-clade enzymes do not necessarily stall if an ATPase-inactive subunit occupies the hydrolysis position. In the Rpt_{1-6} hexamer of the yeast 26S proteasome, for example, ATPase-defective Rpt_3, Rpt_4, or Rpt_6 subunits cause virtually complete loss of degradation activity, whereas ATPase-defective Rpt_1, Rpt_2, and Rpt_5 subunits do not[44]. In the alternating Yta10/Yta12 hetero-hexamer (a Yme1 homolog), a Walker-B mutation in Yta12 prevents ATP hydrolysis in Yta10, as expected for tight subunit-subunit coupling in a strictly sequential mechanism, but a Walker-B mutation in Yta10 does not prevent ATP hydrolysis in Yta12, and a variety of mutations in Yta10 or Yta12 restore machine activity when Yta12 is ATPase defective[45]. In combination, these results suggest that even classic-clade AAA+ proteases need not operate by strictly sequential mechanisms, and that all subunits are not tightly coupled.

To account for the observations that ClpXP takes translocation steps substantially larger than 2 residues, often in kinetic bursts, we propose a model, based on our new structures and established observations, whose main features are illustrated in **Figs. 5b** and **5c**. In our model, ATP hydrolysis can occur with some probability in subunits A, B, C, D, or E. If hydrolysis and/or

product release occurs in subunit A, then a power stroke is generated that moves the subunits from positions ABCDEF to FABCDE (**Fig. 5b**). Thus, the top subunit moves to the bottom position in the spiral, dragging substrate with it. A conformational change of this type is captured in a morph in which subunit A in class 2 is aligned with subunit F in class 4 (**Supplementary movie 3**). As the distance from subunit A to subunit F is ~2.5 nm along the axial channel, translocation steps as large as ~10 residues would be possible, and shorter steps could arise from alternative modes of substrate binding or substrate slipping, as discussed above. We further posit that ATP-hydrolysis events in subunits B, C, D, or E create strain in the spiral without an immediate power stroke. Rather, strain is only released as a power stroke when a formerly internal ADP-bound subunit moves into the A position, potentially generating a burst of power strokes. For example, if one hydrolysis event initially occurred in subunit B and a second hydrolysis event then occurred in subunit A, the second event would generate one power stroke, which would move the ADP-bound subunit B into position A, triggering a second power stroke (**Fig. 5c**). If hydrolysis occurred in subunits B, C, D, and E before hydrolysis occurs in subunit A, then a burst of five power strokes could be generated.

Our model accounts for bursts of translocation steps with sizes similar to those observed experimentally without the need to rebind ATP after each step. It also explains how ClpXP can operate with reasonable efficiency with only two hydrolytically active subunits in the ClpX spiral. For example, if hydrolysis occurred at an ATPase-active subunit B and subunit A were ATPase-inactive, then ATP/ADP exchange in subunit A might trigger the first power stroke. Alternatively, strain in the spiral, generated by the first hydrolysis event, might make it easier for thermal motions to move subunit B into the A position. One potential weakness of our model is that subunits A and F have fewer substrate contacts than subunits B, C, D, and E in our structures. Thus how translocation is coupled to this large conformational shift between the top and bottom

subunits or how substrate contacts with subunits B-E are broken or disengaged during a translocation step is presently unclear.

Structures in the ClpX reaction cycle are likely to be missing, either before or after a power stroke. Crystal structures reveal rotations between the large and small AAA+ domains so large that nucleotide cannot bind some subunits[22,23]. Although subunits of this type are not present in the current cryo-EM structures, they could represent transient functional conformations, as crosslinks engineered to trap these hexamer conformations form in solution and prevent ClpXP degradation but not ATP hydrolysis[23,46]. As noted above, additional modes of ClpX interaction with substrate in the channel must exist to account for ClpX translocation of polyproline. Similarly, multiple polypeptides and knotted proteins can be translocated through the ClpX channel[47–50], but the channel we observe would need to expand substantially to allow multi-chain translocation. Structures of additional conformations of substrate-bound ClpXP should help test the proposed translocation mechanism.

METHODS

Protein expression and purification

The single-chain ClpX variant used for microscopy contained six copies of *E. coli* E185Q ClpX$^{\Delta N}$ (residues 62-424), with neighboring units connected by six-residue linkers of variable composition, and a C-terminal TEV cleavage site and His_6 tag. The ClpP variant consisted of full-length *E. coli* ClpP followed by a TEV cleavage site and His_6 tag. Both proteins were expressed separately in *E. coli* strain ER2566 and purified as described[23]. After purification, TEV protease was used to remove the His_6 tags. TEV protease and uncleaved proteins were removed by Ni^{2+}-NTA affinity chromatography, and purified proteins were flash frozen in storage buffer (20 mM HEPES, pH 7.5, 300 mM KCl, 0.5 mM EDTA, 10% glycerol) and stored at –80 °C.

Sample preparation, data acquisition, and image processing

To assemble complexes, the ClpX$^{\Delta N}$ pseudohexamer and ClpP$_{14}$ were diluted into EM buffer (20 mM HEPES, pH 7.5, 100 mM KCl, 25 mM $MgCl_2$, 5 mM ATPγS) to final concentrations of 4 μM and 1.8 μM, respectively. After 5 min at 25 °C, 3 μL of the mixture was applied to glow discharged R1.2/1.3 400 mesh grids (Quantifoil). Grids were blotted with filter paper 494 (VWR) and plunged into liquid ethane using a Cryoplunge-3 system (Gatan). Electron micrographs were collected using a Talos Arctica with a Gatan K2-Summit direct electron detector in super-resolution mode. High-resolution movies were recorded at a magnification of 36000X (0.58 Å pixel size). Each movie was composed of fifty frames (200 ms per frame) and a total dose of ~58 $e^-/Å^2$ per movie. The final dataset consisted of 3657 movies recorded in two separate sessions. Frames in each movie were 2X binned, aligned, gain-corrected, and dose-weighted using Motioncor2[51], to generate a single micrograph. The contrast transfer function (CTF) was estimated using CTFFIND4[52]. Relion 2.0[53] was used for 2D/3D classification and refinement unless noted.

For initial data analysis, 63,139 particles were picked automatically from a subset of 724 micrographs, using templates generated from 2D classification of ~1000 manually picked doubly capped complexes. After three iterations of 2D classification, 28,004 particles representing side views were selected for subsequent processing. To generate an initial model for 3D refinement, the crystal structures of a ClpX$^{\Delta N}$ hexamer (PDB 3HWS)[22] and a ClpP tetradecamer (PDB code 3MT6)[30] were merged in PyMOL and low-pass filtered to 40 Å. 3D refinement with C_2 symmetry yield a map at a resolution of 6.8 Å.

The limited resolution of the C_2 reconstruction suggested heterogeneity, and thus ClpX$^{\Delta N}$ and ClpP were treated separately. For the ClpP reconstruction, we applied soft circular masks,

including ClpP and the tips of the ClpX IGF loops, to the 3D reference and the 2D images, respectively. Because we observed predominantly side views of ClpXP (perpendicular to the axial channel; **Supplementary Fig. 1**), this simple masking of the particle images allowed us to remove most of the ClpX density and to focus particle alignment on ClpP. Starting from a low-pass filtered ClpP structure as initial reference, 3D refinement with D7 symmetry yielded a 4.2-Å resolution map. For the ClpX reconstruction, we extracted ClpX sub-particles from both ends of ClpP based on the previously determined ClpP alignment using a python script and IMOD[54]. This procedure utilized the original and a ClpP-signal-subtracted stack. To remove misaligned particles, the ClpX stacks were 2D classified without alignment. 51,365 particles were selected as "good" particles from 2D-class averages that showed clear secondary structure. To determine the position of each ClpX hexamer relative to the alignment of the ClpP heptamer, we C_7 symmetry expanded the ClpX particles and 3D classified without alignment. This allowed us to filter $ClpX^{\Delta N}$, which has ambiguous alignment to ClpP, and yielded 48,705 distinct $ClpX^{\Delta N}$ particles. Symmetry-reduced ClpX particles were 3D classified without alignment (K=6) and refined locally with FrealignX[55]. The best class had 8,980 particles and showed clear density from individual alpha helices. As described below, for the final complete dataset, symmetry-expansion, classification without alignment, and local alignment were not required to arrive at meaningful asymmetric ClpX reconstructions. The Relion classification and reconstruction algorithm could converge on high-resolution ClpX structures in the presence of pseudo hexagonal symmetry.

A similar data-processing strategy was applied to the complete dataset. 1.4 million doubly capped particles were automatically picked and filtered by 2D classification. 443,717 "good" particles were selected for map reconstruction. 3D refinement with a small mask and D_7 symmetry yield a ClpP map of 3.2 Å resolution. To extract ClpX sub-particles, the same method using in initial data processing was applied. Clean ClpX sub-particles were 3D classified (K=6)

and refined. This resulted in four distinct ClpX classes with resolutions ranging from 3.9 to 4.2 Å. To recover the ClpX$^{\Delta N}$-ClpP interface, we re-extracted ClpXP sub-particles using a larger box that included the cis ClpP ring. Alignment and classification of each ClpXΔN sub-particle was transferred to corresponding ClpX$^{\Delta N}$/ClpP sub-particle and four classes were refined with local optimization, resulting in four ClpX$^{\Delta N}$/ClpP maps (resolutions 4.0 to 4.3 Å).

Model building and refinement

A ClpP tetradecamer (PDB 3MT6) was docked into the D_7 map using Chimera's "fit to map" function[56]. For ClpX$^{\Delta N}$, six copies of the large and small AAA+ domains (PDB 3HWS) were docked into the map sequentially and refined for three iterations in Chimera. Real-space refinement of docked ClpP and ClpX was performed using PHENIX[57], and model building was performed using COOT[58]. ChimeraX[59], Chimera[56], and PyMOL were used to create figures and movies.

Biochemical assays

All assays were conducted at 37 °C in PD buffer (25 mM HEPES-KOH, pH 7.5, 5 mM $MgCl_2$, 200 mM KCl, 10% glycerol). Experiments were performed in triplicate and reported values are averages ± SD. Degradation of ^{CP7}GFP-ssrA (15 μM) by ClpX$^{\Delta N}$ (0.3 μM hexamer) and $ClpP_{14}$ (0.9 μM) was assayed in the presence of 5 mM ATP and was monitored by loss of fluorescent signal (excitation 467 nm; emission 511 nm). For RKH loop mutants with reduced substrate affinity, degradation was measured at high concentrations of fluorescent substrate, with excitation at an off-peak wavelength (excitation 420 nm; emission 511 nm). Degradation of fluorescein-labeled Arc-st11-ssrA by ClpX$^{\Delta N}$ (0.3 μM hexamer) and $ClpP_{14}$ (0.9 μM) was assayed as described[42]. K_M and V_{max} were determined by fitting the average values of replicates to a hyperbolic equation. ATP hydrolysis rates were measured using a coupled-NADH oxidation assay as described[20], using ClpX$^{\Delta N}$ (0.3 μM hexamer), with or without $ClpP_{14}$ (0.9 μM), and 5

mM ATP. Activation of decapeptide cleavage by ClpP or variants was performed as described[60], using $ClpP_{14}$ (50 nM), RseA decapeptide (15 μM), ATP (5 mM) and a regeneration system, and either $ClpX^{\Delta N}$ (0.5 μM hexamer) or ADEB-2B (100 μM), which was a generous gift from J. Sello (Brown).

ACKNOWLEDGMENTS

Supported by NIH grant GM-101988 (R.T.S) and the Howard Hughes Medical Institute (T.A. Baker; S.C. Harrison). We thank S. Glynn, M. Lang, H. Manning, A. Olivares, and K. Schmitz for helpful discussions and C. Xu and K. Song at the Electron Microscopy Facility at the University of Massachusetts Medical School for advice and data collection.

AUTHOR CONTRIBUTIONS

X.F., S.J., and R.T.S. performed cryo-EM experiments, calculations, and/or model building and refinement. T.A. Bell and B.M.S. performed biochemical experiments. S.P.H., T.A. Baker, and R.T.S. oversaw research. All authors contributed to writing and/or revising the manuscript.

COMPETING FINANCIAL INTERESTS

The authors declare no competing financial interests.

References

1. Erzberger, J.P. & Berger, J.M. Evolutionary relationships and structural mechanisms of AAA+ proteins. *Annu. Rev. Biophys. Biomol. Struct*. **35**, 93–114 (2006).

2. Sauer, R.T. & Baker, T.A. AAA+ proteases: ATP-fueled machines of protein destruction. *Annu. Rev. Biochem*. **80**, 587–612 (2011).

3. Puchades, C., Rampello, A.J., Shin, M., Giuliano, C.J., Wiseman, R.L., Glynn, S.E. & Lander, G.C. Structure of the mitochondrial inner membrane AAA+ protease YME1 gives insight into substrate processing. *Science* **358** p. 6363 (2017).

4. de la Peña, A.H., Goodall, E.A., Gates, S.N., Lander, G.C. & Martin, A. Substrate-engaged 26S proteasome structures reveal mechanisms for ATP-hydrolysis-driven translocation. *Science* **362** pii: eaav0725 (2018).

5. Dong, Y., Zhang, S., Wu, Z., Li, X., Wang, W.L., Zhu, Y., Stoilova-McPhie, S., Lu, Y., Finley, D., Mao, Y. Cryo-EM structures and dynamics of substrate-engaged human 26S proteasome. *Nature* **565**, 49–55 (2019).

6. Majumder, P., Rudack, T., Beck, F., Danev, R., Pfeifer, G., Nagy, I. & Baumeister, W. Cryo-EM structures of the archaeal PAN-proteasome reveal an around-the-ring ATPase cycle. *Proc. Natl. Acad. Sci. USA* **116**, 534–539 (2019).

7. Ripstein, Z.A., Huang, R., Augustyniak, R., Kay, L.E. & Rubinstein, J.L. Structure of a AAA+ unfoldase in the process of unfolding substrate. *eLife* **6**, pii: e25754 (2017).

8. Gates, S.N., Yokom, A.L., Lin, J., Jackrel, M.E., Rizo, A.N., Kendsersky, N.M., Buell, C.E., Sweeny, E.A., Mack, K.L., Chuang, E., Torrente, M.P., Su, M., Shorter, J. & Southworth, D.R. Ratchet-like polypeptide translocation mechanism of the AAA+ disaggregase Hsp104. *Science* **357**, 273–279 (2017).

9. Zehr, E., Szyk, A., Piszczek, G., Szczesna, E., Zuo, X. & Roll-Mecak, A. Katanin spiral and ring structures shed light on power stroke for microtubule severing. *Nat. Struct. Mol. Biol*. **24**, 717–725 (2017).

10. Han, H., Monroe, N., Sundquist, W.I., Shen, P.S. & Hill C.P. The AAA ATPase Vps4 binds ESCRT-III substrates through a repeating array of dipeptide-binding pockets. *eLife* **6** pii: e31324 (2017).

11. Sun, S., Li, L., Yang, F., Wang, X., Fan, F., Yang, M., Chen, C., Li, X., Wang, H.W. & Sui, S.F. Cryo-EM structures of the ATP-bound Vps4(E233Q) hexamer and its complex with Vta1 at near-atomic resolution. *Nat. Commun*. **8**, 16064 (2017).

12. Yu, H., Lupoli, T.J., Kovach, A., Meng, X., Zhao, G., Nathan, C.F. & Li, H. ATP hydrolysis-coupled peptide translocation mechanism of *Mycobacterium tuberculosis* ClpB. *Proc. Natl. Acad. Sci. USA* **115**, E9560-E9569 (2018)..

13. White, K.I., Zhao, M., Choi, U.B., Pfuetzner, R.A. & Brunger, A.T. Structural principles of SNARE complex recognition by the AAA+ protein NSF. *eLife* **7**, pii: e38888 (2018).

14. Rizo, A.N., Lin, J., Gates, S.N., Tse, E., Bart, S.M., Castellano, L.M., DiMaio, F., Shorter, J. & Southworth, D.R. Structural basis for substrate gripping and translocation by the ClpB AAA+ disaggregase. *Nat. Commun*. **10**, 2393 (2019).

15. Aubin-Tam, M.E., Olivares, A.O., Sauer, R.T., Baker, T.A. & Lang, M.J. Single-molecule protein unfolding and translocation by an ATP-fueled proteolytic machine. *Cell* **145**, 257–267 (2011).

16. Maillard, R.A., Chistol, G., Sen, G., Righini, M., Tan, J., Kaiser, C.M., Hodges, C., Martin, A. & Bustamante, C. ClpX(P) generates mechanical force to unfold and translocate its protein substrates. *Cell* **45**, 459–469 (2011).

17. Sen, M., Maillard, R.A., Nyquist, K., Rodriguez-Aliaga, P., Pressé, S., Martin, A. & Bustamante, C. The ClpXP protease unfolds substrates using a constant rate of pulling but different gears. *Cell* **155**, 636–646 (2013).

18. Cordova, J.C., Olivares, A.O., Shin, Y., Stinson, B.M., Calmat, S., Schmitz, K.R., Aubin-Tam, M.E., Baker, T.A., Lang, M.J. & Sauer, R.T. Stochastic but highly coordinated protein unfolding and translocation by the ClpXP proteolytic machine. *Cell* **158**, 647–658 (2014).

19. Olivares, A.O., Kotamarthi, H.C., Stein, B.J., Sauer, R.T & Baker, T.A. Effect of directional pulling on mechanical protein degradation by ATP-dependent proteolytic machines. *Proc. Natl. Acad. Sci. USA* **114**, E6306–E6313 (2017).

20. Martin, A., Baker, T.A. & Sauer, R.T. Rebuilt AAA + motors reveal operating principles for ATP-fuelled machines. *Nature* **437**, 1115–1120 (2005).

21. Hersch, G.L., Burton, R.E., Bolon, D.N., Baker, T.A. & Sauer, R.T. Asymmetric interactions of ATP with the AAA+ $ClpX_6$ unfoldase: allosteric control of a protein machine. *Cell* **121**, 1017–1027 (2005).

22. Glynn, S.E., Martin, A., Nager, A.R., Baker, T.A. & Sauer, R.T. Structures of asymmetric ClpX hexamers reveal nucleotide-dependent motions in a AAA+ protein-unfolding machine. *Cell* **139**, 744–756 (2009).

23. Stinson, B.M., Nager, A.R., Glynn, S.E., Schmitz, K.R., Baker, T.A. & Sauer, R.T. Nucleotide binding and conformational switching in the hexameric ring of a AAA+ machine. *Cell* **153**, 628–639 (2013).

24. Kim, Y.I., Levchenko, I., Fraczkowska, K., Woodruff, R.V., Sauer, R.T. & Baker, T.A. Molecular determinants of complex formation between Clp/Hsp100 ATPases and the ClpP peptidase. *Nat. Struct. Biol*. **8**, 230–233 (2001).

25. Joshi, S.A., Hersch, G.L., Baker, T.A. & Sauer, R.T. Communication between ClpX and ClpP during substrate processing and degradation. *Nat. Struct. Mol. Biol*. **11**, 404-411 (2004).

26. Martin, A., Baker, T.A. & Sauer, R.T. Distinct static and dynamic interactions control ATPase-peptidase communication in a AAA+ protease. *Mol. Cell* **27**, 41–52 (2007).

27. Amor, A.J., Schmitz, K.R., Baker, T.A. & Sauer, R.T. Roles of the ClpX IGF loops in ClpP association, dissociation, and protein degradation. *Protein Sci*. **28**, 756–765 (2019).

28. Brötz-Oesterhelt, H., Beyer, D., Kroll, H.P., Endermann, R., Ladel, C., Schroeder, W., Hinzen, B., Raddatz, S., Paulsen, H., Henninger, K., Bandow, J.E., Sahl, H.G. & Labischinski, H. Dysregulation of bacterial proteolytic machinery by a new class of antibiotics. *Nat. Med*. **11**, 1082–1087 (2005).

29. Kirstein, J., Hoffmann, A., Lilie, H., Schmidt, R., Rübsamen-Waigmann, H., Brötz-Oesterhelt, H., Mogk, A. & Turgay, K. The antibiotic ADEP reprogrammes ClpP, switching it from a regulated to an uncontrolled protease. *EMBO Mol. Med*. **1**, 37–49 (2009).

30. Li, D.H., Chung, Y.S., Gloyd, M., Joseph, E., Ghirlando, R., Wright, G.D., Cheng, Y.Q., Maurizi, M.R., Guarné, A. & Ortega, J. Acyldepsipeptide antibiotics induce the formation of a structured axial channel in ClpP: A model for the ClpX/ClpA-bound state of ClpP. *Chem. Biol*. **17**, 959–969 (2010).

31. Lee, B.G., Park, E.Y., Lee, K.E., Jeon, H., Sung, K.H., Paulsen, H., Rübsamen-Schaeff, H., Brötz-Oesterhelt, H. & Song, H.K. Structures of ClpP in complex with acyldepsipeptide antibiotics reveal its activation mechanism. *Nat. Struct. Mol. Biol*. **17**, 471–478 (2010).

32. Siddiqui, S.M., Sauer, R.T. & Baker, T.A. Role of the processing pore of the ClpX AAA+ ATPase in the recognition and engagement of specific protein substrates. *Genes Dev*. **18**, 369–374 (2004).

33. Farrell, C.M., Baker, T.A. & Sauer, R.T. Altered specificity of a AAA+ protease. *Mol. Cell* **25**, 161–166 (2007).

34. Martin, A., Baker, T.A. & Sauer, R.T. Diverse pore loops of the AAA+ ClpX machine mediate unassisted and adaptor-dependent recognition of ssrA-tagged substrates. *Mol. Cell* **29**, 441–450 (2008).

35. Martin, A., Baker, T.A. & Sauer, R.T. Pore loops of the AAA+ ClpX machine grip substrates to drive translocation and unfolding. *Nat. Struct. Mol. Biol.* **15**, 1147–1151 (2008).

36. Iosefson, O., Nager, A.R., Baker, T.A. & Sauer, R.T. Coordinated gripping of substrate by subunits of a AAA+ proteolytic machine. *Nat. Chem. Biol*. **11**, 201–206 (2015).

37. Iosefson, O., Olivares, A.O., Baker, T.A. & Sauer, R.T. Dissection of axial-pore loop function during unfolding and translocation by a AAA+ proteolytic machine. *Cell Rep*. **12**, 1032–1041 (2015).

38. Rodriguez-Aliaga, P., Ramirez, L., Kim, F., Bustamante, C. & Martin, A. Substrate-translocating loops regulate mechanochemical coupling and power production in AAA+ protease ClpXP. *Nat. Struct. Mol. Biol*. **23**, 974–981 (2016).

39. Bell, T.A., Baker, T.A. & Sauer, R.T. Interactions between a subset of substrate side chains and AAA+ motor pore loops determine grip during protein unfolding. *eLife* **8**, pii: e46808 (2019).

40. Baker, T.A. & Sauer, R.T. ClpXP, an ATP-powered unfolding and protein-degradation machine. *Biochim. Biophys. Acta* **1823**, 15–28 (2012).

41. Glynn, S.E., Nager, A.R., Baker, T.A. & Sauer, R.T. Dynamic and static components power unfolding in topologically closed rings of a AAA+ proteolytic machine. *Nat. Struct. Mol. Biol.* **19**, 616–622 (2012).

42. Bell, T.A., Baker, T.A. & Sauer, R.T. Hinge-linker elements in the AAA+ protein unfoldase ClpX mediate intersubunit communication, assembly, and mechanical activity. *Biochemistry* **57**, 6787–6796 (2018).

43. Barkow, S.R., Levchenko, I., Baker, T.A. & Sauer, R.T. Polypeptide translocation by the AAA+ ClpXP protease machine. *Chem. Biol*. **16**, 605–612 (2009).

44. Beckwith, R., Estrin, E., Worden, E.J. & Martin, A. Reconstitution of the 26S proteasome reveals functional asymmetries in its AAA+ unfoldase. *Nat. Struct. Mol. Biol*. **20**, 1164–1172 (2013).

45. Augustin, S., Gerdes, F., Lee, S., Tsai, F.T., Langer, T. & Tatsuta, T. An intersubunit signaling network coordinates ATP hydrolysis by *m*-AAA proteases. *Mol. Cell* **35**, 574–585 (2009).

46. Stinson, B.M., Baytshtok, V., Schmitz, K.R., Baker, T.A. & Sauer, R.T. Subunit asymmetry and roles of conformational switching in the hexameric AAA+ ring of ClpX. *Nat. Struct. Mol. Biol*. **22**, 411–416 (2015).

47. Burton, R.E., Siddiqui, S.M., Kim, Y.I., Baker, T.A. & Sauer, R.T. Effects of protein stability and structure on substrate processing by the ClpXP unfolding and degradation machine. *EMBO J*. **20**, 3092–3100 (2001).

48. Bolon, D.N., Grant, R.A., Baker, T.A., Sauer, R.T. Nucleotide-dependent substrate handoff from the SspB adaptor to the AAA+ ClpXP protease. *Mol. Cell* **16**, 3433–3350 (2004).

49. San Martín, Á., Rodriguez-Aliaga, P., Molina, J.A., Martin, A., Bustamante, C. & Baez, M. Knots can impair protein degradation by ATP-dependent proteases. *Proc. Natl. Acad. Sci. USA* **114**, 9864–9869 (2017).

50. Sivertsson, E.M., Jackson, S.E. & Itzhaki, L.S. The AAA+ protease ClpXP can easily degrade a $3(_1)$ and a $5(_2)$-knotted protein. *Sci. Rep*. **9**, 2421 (2019).

51. Zheng, S.Q., Palovcak, E., Armache, J., Verba, K.A., Cheng, Y. & Agard, D.A. MotionCor2: anisotropic correction of beam-induced motion for improved cryo-electron microscopy. *Nat. Methods* **14**, 331–332 (2017).

52. Rohou, A. & Grigorieff, N. CTFFIND4: Fast and accurate defocus estimation from electron micrographs. *J. Struct. Biol*. **192**, 216–221 (2015).

53. Kimanius, D., Forsberg, B.O., Scheres, S.H. & Lindahl, E. Accelerated cryo-EM structure determination with parallelisation using GPUs in RELION-2. *eLife* **5**, pii: e18722 (2016).

54. Mastronarde, D.N. & Held, S.R. Automated tilt series alignment and tomographic reconstruction in IMOD. *J. Struct. Biol*. **197**, 102–113 (2017).

55. Lyumkis, D., Brilot, A.F., Theobald, D.L. & Grigorieff, N. Likelihood-based classification of cryo-EM images using FREALIGN. *J. Struct. Biol*. **183**, 377–388 (2013).

56. Pettersen, E.F., Goddard, T.D., Huang, C.C., Couch, G.S., Greenblatt, D.M., Meng, E.C. & Ferrin, T.E. UCSF Chimera--a visualization system for exploratory research and analysis. *J. Comput. Chem*. **25**, 1605–1612 (2004).

57. Adams, P.V., Afonine, G., Bunkoczi, V.B., Chen, I.W., Davis, N., Echols, J.J., Headd, L.W.. Hung, G.J., Kapral, R.W., Grosse-Kunstleve, A.J., McCoy, N.W., Moriarty, R., Oeffner, R., Read, R.J., Richardson, D.C., Richardson, J.S., Terwilliger, T.C. & Zwart, P.H. PHENIX: a comprehensive Python-based system for macromolecular structure solution. *Acta Cryst. D* **66**, 213–221 (2010).

58. Emsley, P. & Cowtan, K. Coot: model-building tools for molecular graphics. *Acta Cryst. D* **60**, 2126–2132 (2004).

59. Goddard, T.D., Huang, C.C., Meng, E.C., Pettersen, E.F., Couch, G.S., Morris, J.H. & Ferrin, T.E. UCSF ChimeraX: Meeting modern challenges in visualization and analysis. *Protein Sci*. **27**, 14–25 (2018).

60. Lee, M.E., Baker, T.A. & Sauer, R.T. Control of substrate gating and translocation into ClpP by channel residues and ClpX binding. *J. Mol. Biol*. **399**, 707–718 (2010).